

Rydberg Atomic Antenna in Strongly Driven Multi-Electron Atoms

Stefanos Carlström^{1,2,*}, Jan Marcus Dahlström^{1,2}, Misha Yu Ivanov^{1,3,4} and Serguei Patchkovskii¹

¹Max-Born-Institut, Max-Born-Straße 2A, 12489 Berlin, Germany

²Department of Physics, Lund University, Box 118, SE-221 00 Lund, Sweden

³Department of Physics, Imperial College London,

South Kensington Campus, SW72AZ London, United Kingdom

⁴Institut für Physik, Humboldt-Universität zu Berlin, Newtonstraße 15, 12487 Berlin, Germany

(Dated: May 2, 2022)

We study the role of intermediate excitations of Rydberg states as an example of Kuchiev’s “atomic antenna” in above-threshold ionization of xenon, in particular their effect on the coherence between the spin-orbit-split states of the ion. We focus on the case of a laser frequency close to resonant with the spin-orbit splitting, where a symmetry (parity) argument would preclude any coherence being directly generated by strong-field ionization. Using *ab initio* simulations of coupled multielectron spin-orbit dynamics in strong laser fields, we show how field-driven rescattering of the trapped Rydberg electrons introduces efficient coupling between the spin-orbit-split channels, leading to substantial coherences, exceeding 10% for some photon energies.

Keywords: Ultrafast spin-orbit interaction, above-threshold ionization, Freeman resonances, atomic antenna, rescattering

Spin-orbit effects are usually neglected in the interaction with strong infrared (IR) fields. Few exceptions include the development of consistent treatment within the R-matrix method [1], recent experiments [2, 3] on imaging the spin-orbit breathing of a hole created by strong-field ionization, and the generation of spin-polarized photoelectrons [4] following the proposal of [5, 6]. In all these cases [2–6], the dipole approximation holds, ensuring that no transitions between the spin-orbit-split states were induced by the incident IR field.

In this Letter we show that, even in the dipole approximation, strong IR fields trigger transitions between the spin-orbit-split states of the ion via a mechanism resembling the “atomic antenna” of Kuchiev [7]. In our case, an active electron driven by strong IR field is trapped into a long-lived Rydberg orbit. Oscillating in the IR field, it transfers the energy to the core via non-dipole electron-electron interaction. This atomic antenna breaks the dynamic symmetry with respect to the polarization of the linearly polarized driving laser field [8]. It thereby induces coherence between the spin-orbit-split states of the ion, reduces the entanglement between the ion and the photoelectron, and manifests itself in the photoelectron spectra.

We consider a xenon atom, initially in the ground state, interacting with an IR pulse with photon energy $\hbar\omega$ close to the spin-orbit splitting of the cation, $\Delta E_{s-o} \approx 1.3\text{ eV}$, $\eta \stackrel{\text{def}}{=} \hbar\omega/\Delta E_{s-o} \sim 1$ (atomic units $\hbar = e = a_0 = m_e = 1$ are used in the following). Our calculations include all relevant electronic excitations (i.e. single excitations/ionizations from $5s_{1/2}$, $5p_{1/2}$, or $5p_{3/2}$ are allowed), and account for spin-orbit coupling effects. We solve the time-dependent Schrödinger equation in the dipole approximation and the length

gauge, for a configuration-interaction singles *Ansatz* that allows single excitation/ionization from a Hartree-Fock (HF) reference [9–14]. The spin-orbit interaction is treated using an energy-consistent relativistic effective-core potential [15] (see [16] for an alternative option, based on the four-component Dirac equation). Ion-resolved above-threshold ionization (ATI) photoelectron spectra are computed [14] using the tSURFF [17–21] and iSURFV [22] techniques. From these spectra, we compute the reduced density matrix $\{\rho_{IJ}\}$, obtained by tracing over the photoelectron degrees of freedom. We then form the normalized *degree of coherence*:

$$\tilde{\rho}_{IJ} \stackrel{\text{def}}{=} \frac{\rho_{IJ}}{\sqrt{\rho_{II}\rho_{JJ}}}, \quad (1)$$

where ρ_{IJ} is the coherence between I and J , and ρ_{II} and ρ_{JJ} are the populations in the ion states I and J , respectively. Further details are given in the Supplementary Information [23].

Let us consider coherence between the spin-orbit-split states of the ion generated by ionization [3, 6, 24–27]. The final state of the system “ion+photoelectron” is

$$\begin{aligned} |\Psi\rangle &= |I\rangle|\chi_I\rangle + |J\rangle|\chi_J\rangle \\ &= (|I\rangle + |J\rangle w)|\chi_I\rangle + |J\rangle(|\chi_J\rangle - w|\chi_I\rangle), \end{aligned} \quad (2)$$

where $w \stackrel{\text{def}}{=} \langle\chi_I|\chi_J\rangle$. Coherent spin-orbit dynamics in the ion requires non-zero overlap between the continuum electron wavepackets correlated to the ionic states $|I\rangle$ and $|J\rangle$, respectively: $w \neq 0$. Perfect overlap $|w| = 1$ corresponds to 100% degree of coherence, since (2) factorizes into

$$|\Psi\rangle = (|I\rangle + |J\rangle)|\chi\rangle.$$

Perfect electron-ion entanglement results for $w = 0$.

By a symmetry argument, zero coherence and perfect entanglement are expected for $\eta = 1$: non-zero coher-

* stefanos@mbi-berlin.de; stefanos.carlstrom@matfys.lth.se

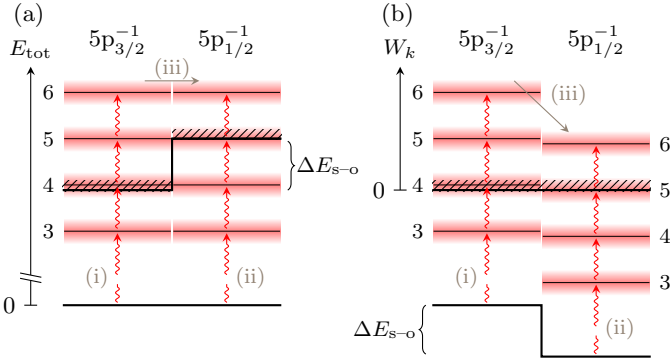


FIG. 1. Sketch of the energy diagram for ATI from xenon for $\eta \stackrel{\text{def}}{=} \hbar\omega/\Delta E_{s-o} = 0.9$; the numbers indicate the amount of photons necessary to reach a certain final energy. The three most important pathways are: (i) direct ionization into the $5p_{3/2}^{-1}$ channel including elastic rescattering, (ii) direct ionization/elastic rescattering in the $5p_{1/2}^{-1}$ channel, and (iii) indirect contributions due to inelastic rescattering from $5p_{3/2}^{-1}$ to $5p_{1/2}^{-1}$ (this dominates over rescattering in the other direction). (a) Total energy (photoelectron + ion), relative to the field-free neutral atom. In this picture, the energy conservation in inelastic scattering is easily seen. (b) Energies of the photoelectrons in each channel. Non-zero photoelectron overlap is necessary for a coherence between the ion cores to exist. For $\eta \sim 1$, photoelectrons of similar kinetic energies are due to absorption of a different number of photons.

ence and hence $w \neq 0$ requires that the two photoelectron wavepackets overlap in energy. After absorption of q photons of energy ω , the photoelectron energy is

$$W_k = q\omega - I_{p,I} - U_p - \frac{\delta\alpha_I}{4}F^2 = q\omega - I_{p,I} - U_p(1 + \omega^2\delta\alpha_I), \quad (3)$$

where ω is the driving laser frequency, $I_{p,I}$ is the ionization potential in ionization channel I , $U_p = F^2/4\omega^2$ the ponderomotive potential of the electric field with peak amplitude F , and $\delta\alpha_I$ the difference between the polarizabilities of the ground state of the neutral and the state of the ion. For $\eta \sim 1$, the photoelectron peaks correlated to the $5p_{3/2}^{-1}$ and $5p_{1/2}^{-1}$ ion cores coincide in energy when one extra photon is absorbed in the $5p_{1/2}^{-1}$ channel (see Figure 1). Thus, the photoelectron associated with $5p_{3/2}^{-1}$ would have opposite parity compared to $5p_{1/2}^{-1}$, while the $5p_{3/2}^{-1}$ and $5p_{1/2}^{-1}$ ion cores have the same parity. The overall parity would thus be opposite between the channels, implying $w = 0$ by symmetry, precluding any coherence. As can be seen from the simulation results in Figure 2, this is not the case; there is non-zero coherence between $5p_{3/2}^{-1}$ and $5p_{1/2}^{-1}$, where the ATI peaks in the respective channels overlap energetically.

Figure 3 shows the calculated degree of coherence (1) between the $5p_{3/2}^{-1}$ and $5p_{1/2}^{-1}$ ion cores, as a function of η . Contrary to the symmetry-based expectation, we see substantial coherence, even exceeding 10% for some η .

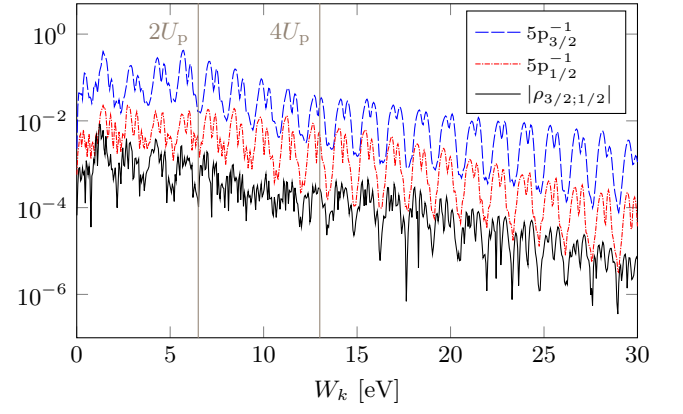


FIG. 2. Calculated ATI spectrum of xenon using $4.4 \times 10^{13} \text{ W cm}^{-2}$ with $\eta \approx 0.96$ and a pulse duration of 30 fs. The dashed blue line is the photoelectron spectrum correlated with the $5p_{3/2}^{-1}$ ionization channel; the dot-dashed red line the corresponding spectrum for the $5p_{1/2}^{-1}$ channel; and the black solid line is the energy-resolved coherence between the two channels. Above approximately $4U_p$, the spectrum in $5p_{1/2}^{-1}$ and the coherence exhibit structures which are very similar to the spectrum in $5p_{3/2}^{-1}$; we infer that the $5p_{1/2}^{-1}$ channel is populated almost exclusively through rescattering in this energy region [see (iii) in Figure 1].

We trace its origin to frustrated tunnelling [28–30] — trapping of the electron into Rydberg states after optical tunnelling from the ground state. Once the neutral atom is “parked” in the intermediate, excited state for an extended amount of time, there is an opportunity to undergo multiple successive (Stokes–)Raman transitions that each increase the system energy by a small amount, while conserving the parity. After multiple such Raman transitions have occurred, the energy may increase enough to bridge the energy gap to the next ATI order. Upon subsequent ionization and rescattering into the other ion channel, the overlap of photoelectrons of the same parity and energy explains the observed coherence.

In the frequency domain, frustrated tunnelling followed by ionization corresponds to the so-called *Freeman resonances* [31] imprinted on top of the photoelectron peaks. The apparent “parity violation” is a manifestation of the dynamic symmetry being broken due to the simultaneous presence of the Freeman resonances, and the spin–orbit interaction. The Freeman resonances introduce memory in the time evolution, breaking time-reversal symmetry, or spatial inversion symmetry between the response of the system to two successive half-cycles. Simultaneously, the spin–orbit coupling leads to the mixing of the ionic spin–orbit channels. Together, these two effects demote the photoelectron parity from a selection rule to a *propensity rule* [8]. We stress that parity conservation of the *whole* wavefunction may *not* be violated, whereas there is no such guarantee for the constituent parts. That parity with respect to the ℓ quantum number of the photoelectron is only a propensity rule has also been observed in

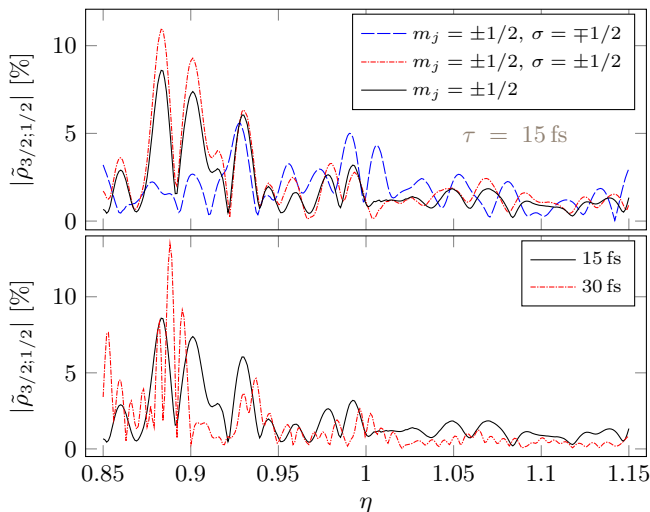


FIG. 3. Ionic coherence in xenon. *Upper panel*: the degree of coherence [Eq. (1)] between the ionization channels $5p_{3/2}^{-1}$ and $5p_{1/2}^{-1}$ as a function of the ratio η between the photon energy and the spin-orbit splitting, resolved on the m_j quantum number of the ion and the spin σ_z of the photoelectron. Due to the cylindrical symmetry of the ionization process, there is a mirror symmetry in the combinations of m_j and σ_z . Additionally tracing out σ_z leads to the final degree of coherence for $m_j = \pm 1/2$, which have the same magnitudes. *Lower panel*: the degree of coherence for two different pulse durations; solid black line: $\tau = 15$ fs, dot-dashed red line: $\tau = 30$ fs.

an analogous example in single-photon spectroscopy of xenon [32, 33], where it has also been linked to the interaction with the core electrons.

The atomic antenna by Kuchiev [7] lends a complementary perspective: the intermediate excited Rydberg states of the neutral are in some aspects very similar to free electrons. A resonance structure is built up in the (Stark-shifted) quasi-continuum of the Rydberg states, that similarly to an antenna can be used to channel energy into the system and thereby drive transitions in the ion core. It is of course necessary that the antenna is “sensitive” to the radiation $\hbar\omega$ impinging on it, such that it may efficiently couple the energy into the system; this is the case if a pair of Rydberg states is separated by $\hbar\omega$. Furthermore, one or both of the states involved in the

TABLE I. Some dipole-allowed transitions in xenon [34] which are likely candidates for the “antenna transition”, given their energies and compositions.

ΔE_{ki} [eV]	i Conf.	Term	k Conf.	Term
1.353	$5p^5(^2P_{3/2})6s$	$2[3/2]_1^\circ$	$5p^5(^2P_{3/2})6p$	$2[3/2]_1$
1.332	$5p^5(^2P_{1/2})6s$	$2[1/2]_1^\circ$	$5p^5(^2P_{3/2})7p$	$2[1/2]_1$
1.265	$5p^5(^2P_{3/2})6s$	$2[3/2]_2^\circ$	$5p^5(^2P_{3/2})6p$	$2[1/2]_1$
1.249	$5p^5(^2P_{3/2})6s$	$2[3/2]_1^\circ$	$5p^5(^2P_{3/2})6p$	$2[5/2]_2$

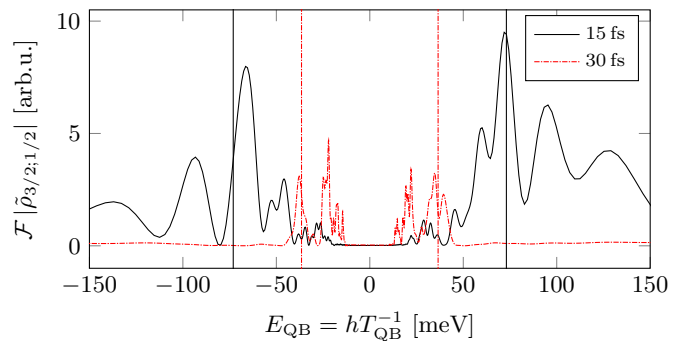


FIG. 4. Fourier transform of the degree of coherence depicted in figure 3, for the two different pulse durations; solid black line: $\tau = 15$ fs, dot-dashed red line: $\tau = 30$ fs. Since $\hbar\omega \equiv \eta\Delta E_{s\rightarrow o}$ has dimension of energy, the conjugate variable has dimension of time. Here, we instead plot the peaks as a function of the quantum beat energy E_{QB} , i.e. the energy separation between neighbouring antenna transitions. The vertical lines indicate the spectral width of the driving pulse, $\delta E = \hbar\sqrt{4\ln 2}\tau^{-1}$, which for $\tau = 15$ fs is ~ 73.1 meV and ~ 36.5 meV for $\tau = 30$ fs.

transition must bridge the ion manifold, i.e. have components in both the $5p_{3/2}^{-1}$ and $5p_{1/2}^{-1}$ manifolds. A few of the likely candidates for the antenna transitions are listed in Table I. This is the frequency-domain perspective of the inelastic rescattering. To confirm the antenna picture, we have investigated transitions for which $\eta \in [0.85, 1.15]$ and their strengths; see the Supplementary Information for details [23].

To further investigate the role of the Rydberg states excited via the Freeman resonances, we perform a Fourier transform of the degree of coherence along the η axis. This analysis reveals quantum beat periods of the excited wavepacket, which constitute a fingerprint of the atomic antenna. By inverting the quantum beat periods, we instead get the energy separation between neighbouring antenna transitions, which is shown in Figure 4. When the pulse duration increases, the spectral bandwidth decreases. This imposes stricter requirements on which antenna transitions are in resonance with the driving field with photon energy $\hbar\omega$. It is more likely to find such transitions among the higher-lying states in the Rydberg quasi-continuum, which are more closely spaced energetically. This explains why for the longer pulse duration, we in Figure 4 observe quantum beat components of the wave packet with comparatively smaller E_{QB} , corresponding to the more tightly spaced peaks in Figure 3.

This circumstance also helps us understand why the longer pulse duration can produce *larger* degrees of coherence, when we might have expected the opposite; decreasing spectral bandwidth leads to narrower photoelectron peaks [35], which in turn leads to smaller energetic overlap between the ATI progressions. However, as long we are in resonance with the antenna, a longer pulse is beneficial since we can transfer population into the different pathways, while maintaining coherence. This is rem-

inherent of the previously studied case of weak-photon ionization of xenon [36], where longer pulse durations also led to increased ionic coherence, albeit for a simpler resonance condition.

We have shown that through the intermediate Rydberg state dynamics, we can introduce coherence between ionization pathways that would otherwise have opposite parity by symmetry. The coherence is sensitive to the frequency and duration of the ionizing laser pulse, and allows one to identify the effect of the Rydberg atomic antenna essentially background-free.

ACKNOWLEDGMENTS

We would like to acknowledge the help of the late Oleg Zatsarinny in estimating the viability of this project. The work of SCM has been supported through scholarship 185-608 from *Olle Engkvists Stiftelse*. JMD acknowledges support from the *Knut and Alice Wallenberg Foundation* (2017.0104 and 2019.0154), the *Swedish Research Council* (2018-03845) and *Olle Engkvists Stiftelse* (194-0734). MI acknowledges support from *Deutsche Forschungsgemeinschaft* and QUTIF grant IV 156-2.

-
- [1] J. Wragg, D. D. A. Clarke, G. S. J. Armstrong, A. C. Brown, C. P. Ballance, and H. W. van der Hart, *Physical Review Letters* **123**, 163001 (2019).
- [2] M. Kübel, Z. Dube, A. Y. Naumov, D. M. Villeneuve, P. B. Corkum, and A. Staudte, *Nature Communications* **10**, 1042 (2019).
- [3] E. Goulielmakis, Z.-H. Loh, A. Wirth, R. Santra, N. Rohringer, V. S. Yakovlev, S. Zherebtsov, T. Pfeifer, A. M. Azzeer, M. F. Kling, S. R. Leone, and F. Krausz, *Nature* **466**, 739 (2010).
- [4] A. Hartung, F. Morales, M. Kunitski, K. Henrichs, A. Laucke, M. Richter, T. Jahnke, A. Kalinin, M. Schöffler, L. P. H. Schmidt, and et al., *Nature Photonics* **10**, 526–528 (2016).
- [5] I. Barth and O. Smirnova, *Physical Review A* **88**, 013401 (2013).
- [6] I. Barth and O. Smirnova, *Journal of Physics B: Atomic, Molecular and Optical Physics* **47**, 204020 (2014).
- [7] M. Y. Kuchiev, *Soviet Journal of Experimental and Theoretical Physics Letters* **45**, 404 (1987).
- [8] M. E. Tzur, O. Neufeld, A. Fleischer, and O. Cohen, *New Journal of Physics* **23**, 103039 (2021).
- [9] R. K. Nesbet, *Proceedings of the Royal Society of London. Series A. Mathematical and Physical Sciences* **230**, 312 (1955).
- [10] P.-O. Löwdin, *Physical Review* **97**, 1474 (1955).
- [11] P. Krause, T. Klamroth, and P. Saalfrank, *The Journal of Chemical Physics* **123**, 074105 (2005).
- [12] N. Rohringer, A. Gordon, and R. Santra, *Physical Review A* **74**, 043420 (2006).
- [13] L. Greenman, P. J. Ho, S. Pabst, E. Kamarchik, D. A. Mazziotti, and R. Santra, *Physical Review A* **82**, 023406 (2010).
- [14] S. Carlström, M. Spanner, and S. Patchkovskii (2022); S. Carlström, M. Bertolino, J. M. Dahlström, and S. Patchkovskii (2022).
- [15] K. A. Peterson, D. Figgen, E. Goll, H. Stoll, and M. Dolg, *The Journal of Chemical Physics* **119**, 11113 (2003).
- [16] F. Zapata, J. Vinbladh, A. Ljungdahl, E. Lindroth, and J. M. Dahlström, *Physical Review A* **105**, 012802 (2022).
- [17] A. M. Ermolaev, I. V. Puzynin, A. V. Selin, and S. I. Vinitsky, *Physical Review A* **60**, 4831 (1999).
- [18] A. M. Ermolaev and A. V. Selin, *Physical Review A* **62**, 015401 (2000).
- [19] V. V. Serov, V. L. Derbov, B. B. Joulakian, and S. I. Vinitsky, *Physical Review A* **63**, 062711 (2001).
- [20] L. Tao and A. Scrinzi, *New Journal of Physics* **14**, 013021 (2012).
- [21] A. Scrinzi, *New Journal of Physics* **14**, 085008 (2012).
- [22] F. Morales, T. Bredtmann, and S. Patchkovskii, *Journal of Physics B: Atomic, Molecular and Optical Physics* **49**, 245001 (2016).
- [23] See Supplementary Information at [URL will be inserted by publisher] for a brief description of the computational details, and a further investigation of the atomic antenna mechanism.
- [24] S. Pabst, M. Lein, and H. J. Wörner, *Physical Review A* **93**, 023412 (2016).
- [25] M. Ruberti, P. Decleva, and V. Averbukh, *Journal of Chemical Theory and Computation* **14**, 4991 (2018).
- [26] M. Ruberti, *Physical Chemistry Chemical Physics* **21**, 17584 (2019).
- [27] M. Ruberti, *Faraday Discussions* **228**, 286 (2021).
- [28] T. Nubbemeyer, K. Gorling, A. Saenz, U. Eichmann, and W. Sandner, *Physical Review Letters* **101**, 233001 (2008).
- [29] U. Eichmann, T. Nubbemeyer, H. Rottke, and W. Sandner, *Nature* **461**, 1261 (2009).
- [30] H. Zimmermann, S. Patchkovskii, M. Ivanov, and U. Eichmann, *Physical Review Letters* **118**, 013003 (2017).
- [31] R. R. Freeman, P. H. Bucksbaum, H. Milchberg, S. Darack, D. Schumacher, and M. E. Geusic, *Physical Review Letters* **59**, 1092 (1987).
- [32] D. Dill, *Physical Review A* **7**, 1976 (1973).
- [33] J. A. R. Samson and J. L. Gardner, *Physical Review Letters* **31**, 1327 (1973).
- [34] E. B. Saloman, *Journal of Physical and Chemical Reference Data* **33**, 765 (2004).
- [35] G. Petite, P. Agostini, and F. Yergeau, *Journal of the Optical Society of America B* **4**, 765 (1987).
- [36] S. Carlström, J. Mauritsson, K. J. Schafer, A. L’Huillier, and M. Gisselbrecht, *Journal of Physics B: Atomic, Molecular and Optical Physics* **51**, 015201 (2018).

SUPPLEMENTARY INFORMATION

We employ Hartree atomic units and implied summation/integration over indices, orbitals, momenta, and/or spins appearing on only one side of an equation.

1. Grid-Based Time-Dependent Configuration Interaction Singles

The derivation of the equations of motion (EOMs), and a detailed description of the propagator are given in [14]; the EOMs agree with those of Rohringer *et al.* [12] and Greenman *et al.* [13], apart from the fact that spin-restriction is *not* imposed in the present work, i.e. we are solving the two-component Schrödinger equation.

The TD-CIS EOMs describe the time evolution of the amplitude c_0 for the Hartree–Fock (HF) reference state, and the particle orbital $|\tilde{k}\rangle$ emanating from the occupied (time-independent) orbital $|k\rangle$. The different particle–hole channels can couple via either the laser interaction or the Coulomb interaction:

$$\begin{aligned} i\partial_t c_0 &= \langle k|\hat{V}_L|\tilde{k}\rangle, \\ i\partial_t |\tilde{k}\rangle &= (-\epsilon_k + \hat{f})|\tilde{k}\rangle + c_0\hat{V}_L|k\rangle - \langle l|\hat{V}_L|k\rangle|\tilde{l}\rangle \\ &\quad - (\hat{J}_{lk} - \hat{K}_{lk})|\tilde{l}\rangle - \lambda_{\tilde{k}i}|i\rangle, \end{aligned} \quad (\text{SI-1})$$

where ϵ_k is the energy of the occupied orbital $|k\rangle$, the Fock operator is defined as $\hat{f} \stackrel{\text{def}}{=} \hat{h} + \hat{J}_{ii} - \hat{K}_{ii}$, with the one-body Hamiltonian containing the interaction with the external laser field, $\hat{h} \stackrel{\text{def}}{=} p^2/2 + \hat{V}_C(\mathbf{r}) + \hat{V}_L$, $\hat{V}_L \stackrel{\text{def}}{=} \mathbf{F}(t) \cdot \mathbf{r}$, and the *direct* and *exchange interaction* potentials are given by their action on an orbital

$$\begin{aligned} \hat{J}_{cd}|e\rangle &\stackrel{\text{def}}{=} \chi_e(\varsigma_1) \int \frac{d\varsigma_2}{|\mathbf{r}_1 - \mathbf{r}_2|} \chi_c^*(\varsigma_2) \chi_d(\varsigma_2), \\ \hat{K}_{cd}|e\rangle &\stackrel{\text{def}}{=} \chi_d(\varsigma_1) \int \frac{d\varsigma_2}{|\mathbf{r}_1 - \mathbf{r}_2|} \chi_c^*(\varsigma_2) \chi_e(\varsigma_2) \equiv \hat{J}_{ce}|d\rangle, \end{aligned}$$

where $\varsigma_{1,2}$ refer to both spatial and spin coordinates of the orbitals. As we consider atoms in the present work, the particle orbitals $|\tilde{k}\rangle|\tilde{l}\rangle\dots$ are conveniently expanded in a tensor product basis formed from spinor spherical harmonics [i.e. $n\ell j m_j$; see §7.2 of SI1] and finite-differences for the radial dimension [SI2, SI3]. Finally, the Lagrange multiplier $\lambda_{\tilde{k}i}$ ensures that $|\tilde{k}\rangle$ at all times remains orthogonal to the occupied orbital $|i\rangle$.

Because we are working in the dipole approximation, \hat{V}_L includes E_1 transitions only. As discussed in the main text, $5p_{3/2}^{-1}$ and $5p_{1/2}^{-1}$ have the same parity, which means $\langle 5p_{3/2}^{-1}|\hat{V}_L|5p_{1/2}^{-1}\rangle = 0$. However, even if the dipole-forbidden (E_2 and M_1) transitions between $5p_{3/2}^{-1}$ and $5p_{1/2}^{-1}$ were to be included, they would be so minuscule [SI4, SI5] that the resulting coherence would be 10^{-7} to 10^{-9} . Instead, in our simulations we find coherence $\sim 10^{-2}$ for *all* $\eta \sim 1$.

2. Atomic Structure and Pulse Parameters

The EOMs (SI–1) as formulated would yield the same result as a one-component calculation, i.e. there would be no effect due to the spin of the electrons. To implement spin–orbit coupling (as well as corrections due to scalar-relativistic effects), and at the same time reducing the number of electrons we need to treat in the calculation, we replace the scalar potential \hat{V}_C by the relativistic effective core potential (RECP) of Peterson *et al.* [15], which models the nucleus and the 1s–3d electrons according to

$$\hat{V}_{\text{PP}}(\mathbf{r}) = -\frac{Q}{r} + B_{\ell j}^k \exp(-\beta_{\ell j}^k r^2) \hat{P}_{\ell j},$$

where $Q = 26$ is the residual charge, $\hat{P}_{\ell j}$ is a projector on the spin–angular symmetry ℓj , and $B_{\ell j}^k$ and $\beta_{\ell j}^k$ are numeric coefficients found by fitting to multiconfigurational Dirac–Fock all-electron calculations of the excited spectrum. For a thorough introduction to RECPs, see e.g. the review by Dolg and Cao [6].

The radial grid consists of 527 points extending to 90.4 Bohr with the spacing smoothly varying according to [SI3]:

$$r_j = r_{j-1} + \rho_{\min} + (1 - e^{-\alpha r_{j-1}})(\rho_{\max} - \rho_{\min}),$$

with $r_1 = \rho_{\min}/2$, $\rho_{\min} = 0.1154$ Bohr, $\rho_{\max} = 0.1768$ Bohr, and $\alpha = 0.3$. The spin–angular grid is limited to $\Delta m_j = 0$ since we only consider linearly polarized light. For pulses of duration 15 fs we use $\ell_{\max} = 40$, and for 30 fs $\ell_{\max} = 60$.

Finally, since the calculation is performed in a finite computational domain, we use Manolopoulos’ [SI7] transmission-free *complex-absorbing potential* covering the last 12.57 Bohr at the far end of the box, with a design parameter $\delta \approx 0.21$; this choice gives $< 1\%$ reflection for photoelectrons with kinetic energies above 3.4 eV ($\iff k_{\min} = 0.5$ au).

TABLE II. Calculated ionization potentials of the 5p electrons of xenon, compared with their experimental values. The corresponding Keldysh parameters, for the range of pulse energies used, indicate that ionization is in a regime intermediate between the multi-photon and tunneling limits.

Hole	I_p [eV]	Exp. [34] [eV]	Δ [eV]	Keldysh γ
$5p_{1/2}^{-1}$	13.483	13.436	0.047	1.28–1.73
$5p_{3/2}^{-1}$	12.026	12.130	–0.104	1.21–1.63

With these grid parameters, the ionization potentials for the xenon model (only 5s and 5p orbitals are allowed to ionize) are given in Table II; the calculated spin–orbit splitting is approximately $\Delta E_{s-o} \approx 1.46$ eV. The driving field frequency is scanned across the range $\eta \stackrel{\text{def}}{=} \hbar\omega/\Delta E_{s-o} \in [0.85, 1.15] \implies \hbar\omega = 1.24$ eV to 1.68 eV, and its intensity $I_0 = 4.4 \times 10^{13}$ W cm $^{-2} \implies U_p = 4.12$ eV to 2.25 eV is chosen such that the ionization

remains at the level of a few percent. The pulse duration is 15 fs or 30 fs, and the pulse shape is a smoothly truncated Gaussian [S18], with $t_1 = 25.5$ fs, $t_2 = 38.2$ fs and $t_1 = 51.0$ fs, $t_2 = 76.4$ fs, respectively. The time propagator is second-order accurate, and 2000 steps per carrier cycle are taken, which yields a time step τ varying from 1.67 as to 1.23 as, for the range of values of η quoted above.

3. Photoelectron Spectra and Ion Coherences

Photoelectron spectra are computed using a multichannel extension [14] of the tSURFF [17–21] and iSURFV [22] techniques, yielding the familiar close-coupling [S19] decomposition of the wavefunction, resolved on final ion state I , and photoelectron momentum \mathbf{k} and spin σ_z (it is assumed that the ion and photoelectron sufficiently separated, such that antisymmetrization can be safely omitted):

$$|\Psi\rangle = c_{I\mathbf{k}\sigma_z} |I\rangle |\mathbf{k}\sigma_z\rangle.$$

From this long-range *Ansatz*, we can form the density matrix of the total system

$$\hat{\rho}_{I\mathbf{k}'\sigma'_z; J\mathbf{k}''\sigma''_z} \stackrel{\text{def}}{=} |\Psi\rangle\langle\Psi| = c_{I\mathbf{k}'\sigma'_z} |\mathbf{k}'\sigma'_z\rangle \langle I| \langle J| \langle \mathbf{k}''\sigma''_z| c_{J\mathbf{k}''\sigma''_z}^*,$$

and by subsequently tracing out the photoelectron, the *reduced density matrix*, expressing the coherence between ion states

$$\rho_{IJ} = \langle \mathbf{k}\sigma_z | \langle I | \hat{\rho} | J \rangle | \mathbf{k}\sigma_z \rangle = c_{I\mathbf{k}\sigma_z} c_{J\mathbf{k}\sigma_z}^*,$$

(the population for the ion state I is $\rho_I \equiv \rho_{II}$). These quantities are used to compute the degree of coherence as shown in Eq. (1).

4. Confirming the Atomic Antenna

Below, we will discuss various aspects of the atomic antenna [7], and various avenues we have pursued to confirm that this proposed mechanism is indeed responsible for the observed symmetry breaking and hence non-vanishing coherence in the energy regime where we would expect to see nothing, due to the absorption of different number of photons.

a. Influence of Depletion

Since the degree of coherence is on the order of a few percent, similar to the level of ionization for the intensity chosen, an alternative explanation could be depletion-induced residual coherence. This would be a memory effect, similar to hole-burning, deviating from the cycle-cycle adiabaticity and breaking the time-symmetry [S10, S11]. To rule out this possibility, we artificially

prevented the depletion of the ground state by renormalizing the ground state amplitude after every time step, which did not change the final coherence.

b. Dynamical Effects due to the Envelope

We also investigated whether the dynamical AC Stark shift of the Rydberg states due to the envelope of the laser field had any influence on the coherence. Substituting the Gaussian envelope by a flattop pulse, removes most of the dynamical shifts, leaving only a constant AC Stark shift. The degree of coherence was mostly unaffected by this, only increasing by a few percent.

c. Removing one Rydberg State

We begin by confirming that the Rydberg states, populated via frustrated tunnelling, are important in the formation of the antenna. To test this hypothesis we repeated the calculation, while preventing the $5p_{3/2}^{-1}$ 6s state from being intermediately excited *via the laser interaction*. The propagator \mathcal{U}_L for the laser interaction \hat{V}_L is replaced according to

$$\mathcal{U}_L \rightarrow \hat{P}\mathcal{U}_L\hat{P} + \hat{Q}, \quad (\text{SI-2})$$

where \hat{Q} is the projector onto the $5p_{3/2}^{-1}$ 6s state and $\hat{P} \equiv \hat{1} - \hat{Q}$ is the projector onto the orthogonal complement. In this way, the $5p_{3/2}^{-1}$ 6s state is still present in the calculation, but it will not be coupled via the laser field; we can do this since in the length gauge, the field-free excited state remains a good approximation to the time-dependent eigenstate. The state chosen has ~ 0.979 contribution from the $5p_{3/2}^{-1}$ manifold, $\sim 1.95 \times 10^{-2}$ contribution from $5p_{1/2}^{-1}$, and $\sim 1.82 \times 10^{-3}$ contribution from

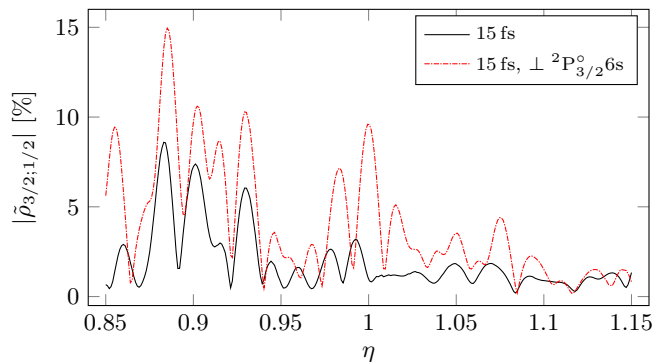


FIG. 5. Effect on the degree of coherence by removing $5p_{3/2}^{-1}$ 6s from the calculation, see Equation (SI-2); black, solid line, the degree of coherence for a 15 fs pulse (same as seen in Figure 3 of the main article), and red, dot-dashed line, the degree of coherence for the same pulse, but with $5p_{3/2}^{-1}$ 6s projected out.

$5s_{1/2}^{-1}$ through configuration interaction, which makes it a likely candidate for the antenna mechanism.

As we see in Figure 5, the degree of coherence is strongly altered by the removal of $5p_{3/2}^{-1} 6s$, confirming the importance of the Rydberg states in the formation of the antenna. The exact influence of individual states on the antenna efficiency and the final coherence is a topic for future investigations.

d. Antenna Transition Strength

We now would like to investigate whether there is a correlation between the transitions in the Rydberg manifold that constitute our antenna, and the observed variation of the degree of coherence $\tilde{\rho}_{3/2;1/2}$ with the photon energy. The weight of the antenna transition between states a and b is estimated as

$$w_{ab} = |z_{ab}|^2 [\min(|c_{3/2}^{(a)}|^2, |c_{1/2}^{(a)}|^2) + \min(|c_{3/2}^{(b)}|^2, |c_{1/2}^{(b)}|^2)], \quad (\text{SI-3})$$

where $c_J^{(s)}$ is the complex amplitude of state s in channel J . Diagonalizing the field-free Hamiltonian [(SI-1) with $\hat{V}_L = 0$], we obtain the first 150 excited states, and compute (SI-3) for all dipole-allowed transitions. Those that fall within the energy interval we consider, are shown as a stick spectrum in Figure 6, alongside the degree of coherence. By convoluting the stick spectrum with a Lorentzian

$$\Lambda(\omega) = \frac{1}{1+x^2}, \quad x = \frac{2\omega}{\Gamma}, \quad (\text{SI-4})$$

where Γ is the full width at half maximum, a continuous distribution is acquired; we use $\Gamma = 5 \times 10^{-4}$ Ha, $h/\Gamma \sim 48$ fs. The similarity of the convoluted spectrum with the degree of coherence is very suggestive, apart

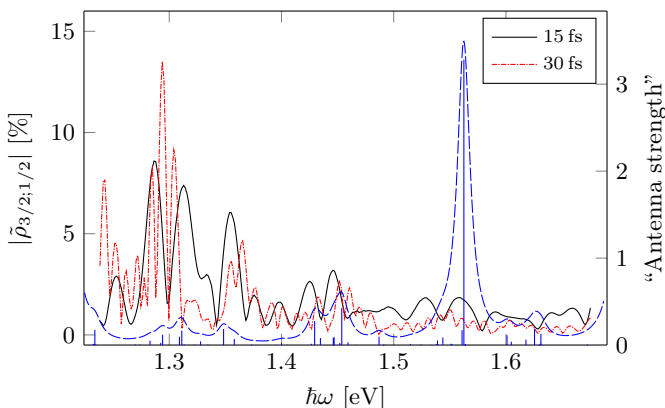


FIG. 6. Antenna transitions: The left ordinate corresponds to the degree of coherence for 15 fs and 30 fs are shown in solid black and dot-dashed red lines, respectively. The right ordinate corresponds to the antenna strengths, computed using (SI-3) and shown as sticks, and convoluted with a Lorentzian spectral shape (SI-4), shown as the dashed blue line.

from the very strong peak at ~ 1.56 eV, which is due to a very strong dipole moment for that transition. Exact agreement can, however, not be expected for a variety of reasons. Equation (SI-3) considers dipole transitions between field-free states, i.e. disregarding any Stark shifts in the strong field, which means the transitions might not occur at the positions indicated. More important, though, is the fact that we completely disregard the relative populations of the constituent states, which, when prepared through frustrated tunnelling depend strongly on the laser parameters [28].

e. Antenna Size

Finally, we want to estimate the effective size of the antenna structure, and relate that to the driving wavelength. In classical electromagnetic theory, a dipole antenna will exhibit the largest gain if the length is $5\lambda/4$; $\lambda/2$ is also very common. Naturally, electron excursions on that scale would far exceed the applicability of the dipole approximation, however, this gives a clear motivation for why large electronic structures are desirable to efficiently couple the external electric field into the atom.

An excited state can in the CIS Ansatz be written as

$$\sum_k \tilde{\Phi}_k,$$

with the particle orbital $|\tilde{k}\rangle$ containing all information about the electron in the channel associated with excitation/ionization from the occupied orbital $|k\rangle$. We estimate the size of the state as

$$s_1 \stackrel{\text{def}}{=} \sqrt{\sum_k \langle \tilde{k} | r^2 | \tilde{k} \rangle}; \quad s_2 \stackrel{\text{def}}{=} \sum_k \sqrt{\langle \tilde{k} | r^2 | \tilde{k} \rangle}.$$

The size of the antenna is then estimated as the geometric mean of the sizes of the two states:

$$\sqrt{s(a)s(b)}$$

For the transitions in Figure 6, the estimates fall in the range 1 nm to 3 nm, and with a driving wavelength of $\lambda \sim 900$ nm, this corresponds to $\frac{\lambda}{900} - \frac{\lambda}{300}$ antenna structures. This is of course far from the optimum $\frac{5\lambda}{4}$, but a lot better than what could be expected from the orbitals of the ground state; $5\{s, p\}$ have a size of ~ 0.1 nm which would yield a $\frac{\lambda}{9000}$ antenna.

References

- [SI1] D. A. Varshalovich, *Quantum Theory of Angular Momentum: Irreducible Tensors, Spherical Harmonics, Vector Coupling Coefficients, 3nj Symbols* (World Scientific Pub, Singapore Teaneck, NJ, USA, 1988).
- [SI2] S. L. Adler and T. Piran, *Reviews of Modern Physics* **56**, 1 (1984).

- [SI3] J. L. Krause and K. J. Schafer, *The Journal of Physical Chemistry A* **103**, 10118 (1999).
- [SI4] R. Garstang, *Journal of Research of the National Bureau of Standards Section A: Physics and Chemistry* **68A**, 61 (1964).
- [SI5] D. K. Nandy and B. K. Sahoo, *Monthly Notices of the Royal Astronomical Society* **450**, 1012 (2015).
- [SI6] M. Dolg and X. Cao, *Chemical Reviews* **112**, 403 (2011).
- [SI7] D. E. Manolopoulos, *J. Chem. Phys.* **117**, 9552 (2002).
- [SI8] S. Patchkovskii and H. Muller, *Computer Physics Communications* **199**, 153 (2016).
- [SI9] W. Fritsch and C.-D. Lin, *Physics Reports* **202**, 1 (1991).
- [SI10] R. Jankowiak, J. M. Hayes, and G. J. Small, *Chemical Reviews* **93**, 1471 (1993).
- [SI11] E. Goll, G. Wunner, and A. Saenz, *Physical Review Letters* **97**, 103003 (2006).